Journal of Energy Chemistry 74 (2022) 121–127

Contents lists available at ScienceDirect

Journal of Energy Chemistry

journal homepage: www.elsevier.com/locate/jechem

http://www.journals.elsevier.com/journal-of-energy-chemistry/

Research article

Nanoconfinement effect of nanoporous carbon electrodes for ionic liquid-based aluminum metal anode

Juhee Yoon [a,b], Seongbak Moon [a,b], Son Ha [c], Hyung-Kyu Lim [d,*], Hyoung-Joon Jin [a,b,*], Young Soo Yun [c,e,*]

[a] Program in Environmental and Polymer Engineering, Inha University, Incheon 22212, South Korea
[b] Department of Polymer Science and Engineering, Inha University, Incheon 22212, South Korea
[c] KU-KIST Graduate School of Converging Science and Technology, Korea University, Seoul 02841, South Korea
[d] Division of Chemical Engineering and Bioengineering, Kangwon National University, Gangwon-do 24341, South Korea
[e] Department of Integrative Energy Engineering, Korea University, Seoul 02841, South Korea

ARTICLE INFO

Article history:
Received 6 April 2022
Revised 24 June 2022
Accepted 27 June 2022
Available online 2 July 2022

Keywords:
Nanoconfinement effect
Nanoporous carbon
Ionic liquid electrolyte
Metal anode
Aluminum batteries
Multivalent batteries

ABSTRACT

Rechargeable aluminum batteries (RABs), which use earth-abundant and high-volumetric-capacity metal anodes (8040 mAh cm^{-3}), have great potential as next-generation power sources because they use cheaper resources to deliver higher energies, compared to current lithium ion batteries. However, the mechanism of charge delivery in the newly developed, ionic liquid-based electrolytic system for RABs differs from that in conventional organic electrolytes. Thus, targeted research efforts are required to address the large overpotentials and cycling decay encountered in the ionic liquid-based electrolytic system. In this study, a nanoporous carbon (NPC) electrode with well-developed nanopores is used to develop a high-performance aluminum anode. The negatively charged nanopores can provide quenched dynamics of electrolyte molecules in the aluminum deposition process, resulting in an increased collision rate. The fast chemical equilibrium of anionic species induced by the facilitated anionic collisions leads to more favorable reduction reactions that form aluminum metals. The nanoconfinement effect causes separated nucleation and growth of aluminum nanoparticles in the multiple confined nanopores, leading to higher coulombic efficiencies and more stable cycling performance compared with macroporous carbon black and 2D stainless steel electrodes.

1. Introduction

Rechargeable multivalent batteries (RMBs), which are based on Zn, Mg, or Al cationic charge carriers, have attracted great attention as candidates for next-generation lithium ion batteries (LIBs) because of their high-performance metal anodes, which have better chemical stabilities and much higher volumetric capacities (Mg: 3830, Zn: 5850, and Al: 8040 mAh cm^{-3}) than those (graphite: ~840 and Li: ~2060 mAh cm^{-3}) of rechargeable lithium batteries [1–5]. However, a passivation oxide layer is spontaneously formed on the metal surface in conventional organic electrolytes, which significantly hinders charge delivery [4,6]. This means that new chemistry targeted towards RMBs is needed to achieve better electrochemical performance. In rechargeable aluminum batteries with high-energy metal anodes, substituting an organic electrolyte into an ionic liquid-based system with an aluminum-including anion charge carrier has been used to address the challenge created by the passivation layer [7]. The organic solvent-free electrolyte did not produce oxide layers on the metallic anode surfaces, which led to reversible aluminum metal deposition-dissolution cycles with high coulombic efficiency (CE) [2,8]. Accordingly, high-performance aluminum batteries based on the reversible aluminum metal anode (AMA) have been reported with several different types of cathode materials such as graphitic materials, conductive polymers, vanadium oxides, CuSe, Se, and amine [9–15]. However, because the complex reduction of aluminum progresses via four anion molecules and three electrons, as shown in equation (1), this reaction suffers from large overpotentials, particularly from concentration polarization [16].

$$4Al_2Cl_7^- + 3e^- \rightarrow 7AlCl_4^- + Al \quad (1)$$

In addition, the ionic liquid cations hinder mass transfer of the aluminum ion charge carriers by forming electrochemical double layers on the polarized electrode surfaces under an electric field

* Corresponding authors.
E-mail addresses: hklim@kangwon.ac.kr (H.-K. Lim), hjjin@inha.ac.kr (H.-J. Jin), c-ysyun@korea.ac.kr (Y.S. Yun).

https://doi.org/10.1016/j.jechem.2022.06.048
2095-4956/

[17,18]. The large concentration polarization causes diffusion-controlled metal reduction, leading to dendritic metal growth [19–22]. Owing to the severe problems with dendrite formation, such as safety hazards caused by short-circuits and performance degradation, many researchers have introduced 3D-structured electrode materials with high specific surface areas to address this obstacle [23–27]. Stereoscopic electrode materials can reduce the effective current and accommodate large amounts of electrolytic solution [28]. Moreover, the infinite volume expansion of metal deposition-dissolution cycles can be mitigated, leading to more stable cycle lives [28]. Nevertheless, these strategies are insufficient because the anion-guided deposition of aluminum requires an increase in the anion concentration and an active surface for anion charge carriers. Furthermore, because of the adsorbed cation charge carriers, the large surfaces of the 3D-structured electrode materials are prone to blockage. Hence, building a better AMA requires an electrode design that is more suited to the reaction mechanism.

Herein, we demonstrate that highly efficient and stable aluminum metal deposition/dissolution reactions can be guided with a nanoporous carbon (NPC) electrode by nanoconfinement of the ionic liquid-based charge carriers in the well-ordered nanopores, which are a few nanometers in diameter. The superior electrochemical performance of the NPC electrode is revealed by comparison with macroporous carbon black (CB) and 2D stainless steel (SS) electrodes, where the NPC electrode affords higher CEs and more stable cycling performance. Reversible aluminum nanometalling and dissolution in the confined nanopores are demonstrated through *ex situ* field-emission transmission electron microscopy (FE-TEM) and *ex situ* nitrogen adsorption/desorption isotherm analyses. Moreover, molecular dynamics (MD) simulations were performed to discover the origin of the enhanced electrochemical performance on the NPC electrode. This report is the first to demonstrate that (1) the concentration polarization of the ionic liquid-based charge carrier for the storage of aluminum can be significantly mitigated, and (2) better cycling efficiencies can be achieved by exploiting the nanoconfinement effect of the NPC electrode.

2. Results and discussion

A previously reported template method, where the primary particles had rod-like morphologies with a length of a few micrometers and diameter of 100–200 nm (Fig. 1a and b), was used to fabricate the NPC [29]. The rod-shaped particles were composed of well-ordered nanopores with uniform pore sizes (Fig. 1c and d and Fig. S1). The IUPAC type-IV nitrogen adsorption–desorption isotherms of NPC revealed the mesoporous structure (Fig. 1e), having well-developed pores with a very narrow pore size distribution centered around ~4 nm (Fig. 1f). The specific surface area of the NPC was ~1075 $m^2 g^{-1}$, with a pore volume of ~1.19 $cm^3 g^{-1}$. Considering the high volumetric capacity (~8040 mAh cm^{-3}) of aluminum, an absolute capacity of approximately 9.6 mAh can be stored in the nanopores when 1 mg of NPC is loaded onto 1 cm^{-2}. This simple calculation indicates that the NPC can deliver sufficient charge for the AMA by accommodating aluminum metals in the nanopores.

X-ray diffraction (XRD) and Raman spectroscopy were used to investigate the microstructures of the NPCs. Very broad graphite (002) and (100) peaks were observed at 22.5° and 43.4°, respectively, in the XRD pattern, indicating that the NPCs had poor graphitic ordering (Fig. 1g). The Raman spectrum also exhibited a very broad 2D band at ~2820 cm^{-1}, which further indicates that the graphitic structure was poorly ordered. The two bands of intrinsic carbon, which originated from the disordered A_{1g} breathing mode (*D* band) and the E_{2g} vibration mode of hexagonal carbon structures (*G* band), had similar intensities, indicating that the carbon structure had numerous topological defects [30]. The deconvoluted *D*-to-*G* band intensity ratio (I_D/I_G) was used to compare the detailed carbon bands from the fused *D* and *G* bands. The I_D/I_G value of the NPC is ~1.8, indicating that the NPC has not well-ordered carbon structures.

X-ray photoelectron spectroscopy (XPS) was used to characterize the chemical structures of the NPCs. The peak of the sp^2-hybridized carbon–carbon bond in the deconvoluted XPS C 1*s* profile indicates that the double bond was the major chemical structure of the NPCs (Fig. 1i). An intense peak of sp^3-hybridized carbon, corresponding to the carbon–carbon single bond was also observed, consistent with the Raman spectral data, which indicated the presence of defect carbon structures. Two distinctive oxygen functional groups, namely the carbon–oxygen single and double bond configurations, were also observed in the higher binding energy regions. The O 1*s* XPS profiles showed a more specific oxygen-carbon bond configuration, confirming the presence of ether/hydroxide, carbonyl, and carboxylic acid groups, and the relative intensities indicated that the carbonyl group was the major oxygen functional group (Fig. 1j). The O/C ratio of the NPC was ~0.04. Despite the low oxygen content, it is considered that sufficient polarity was present to interact with the polar electrolyte.

CB, called as Super P, was used as a control sample (Fig. S3). CB had a macroporous structure with a specific surface area and pore volume of ~53 $m^2 g^{-1}$ and 0.07 $cm g^{-1}$, respectively, which correspond to 1/20 and 1/17 for those of NPCs. Because of the clear difference in the pore structures, effects of nanopores on aluminum metal deposition-dissolution processes can be elucidated through comparison of electrochemical performances of the CB and NPC electrodes. Additionally, a carbon-free stainless steel (SS) substrate was used as a control sample to compare the positive effect of carbon-based electrode materials on the AMA.

The electrochemical performance of AMAs employing NPC, CB, and SS was tested in an electrolytic mixture of $AlCl_3$ and ethyl-3-methylimidazolium tetrachloroaluminate ($EMImAlCl_4$) (1.0:1.3 molar ratio), with a cut-off capacity of 1 mAh g^{-1}. The profiles for the galvanostatic deposition of aluminum on the electrodes show the voltage overshooting which is induced by nucleation overpotential (η_n) at ~50 μA cm^{-2} (Fig. 2a). This observation was closely related to the activation energy for forming the metal phase from the ions, as shown in Fig. S4. The η_n values of the NPC, CB, and SS electrodes were ~7.1, ~24.4, and ~73.6 mV, respectively, where the NPC electrode has the lowest η_n value, indicating that this electrode catalyzes the nucleation of aluminum most effectively. In addition, the electrochemical overpotential (η_e) of the NPC electrodes was much smaller than that of the CB and SS electrodes. The initial η_e mainly originated from the ohmic polarization, where a lower η_e value indicates a lower effective current density (Fig. S5). The cyclic voltammograms acquired in the voltage range of 0.01–0.7 V vs. Al^{3+}/Al show that the NPC electrodes had much higher capacitance values. This indicates that the NPC electrodes possess much higher electrochemical active surface areas than those of the CB and SS electrodes (Fig. S6). The profiles for the galvanostatic deposition-dissolution of aluminum, which were acquired at areal current densities of 0.5–3.0 mA cm^{-2}, exhibited large differences in the η_e values at different areal current densities (Fig. 2b–d). Simultaneously, the voltage for reducing aluminum in the CB and SS electrodes gradually decreased with the state of charge (SoC), while the SS electrode showed large voltage drops at the end of the SoC, which occurred more quickly as the areal current densities increased. This dramatic voltage drop is due to concentration polarization. A lack of aluminum anion charge carriers can cause a diffusion-controlled reaction that is accompanied by

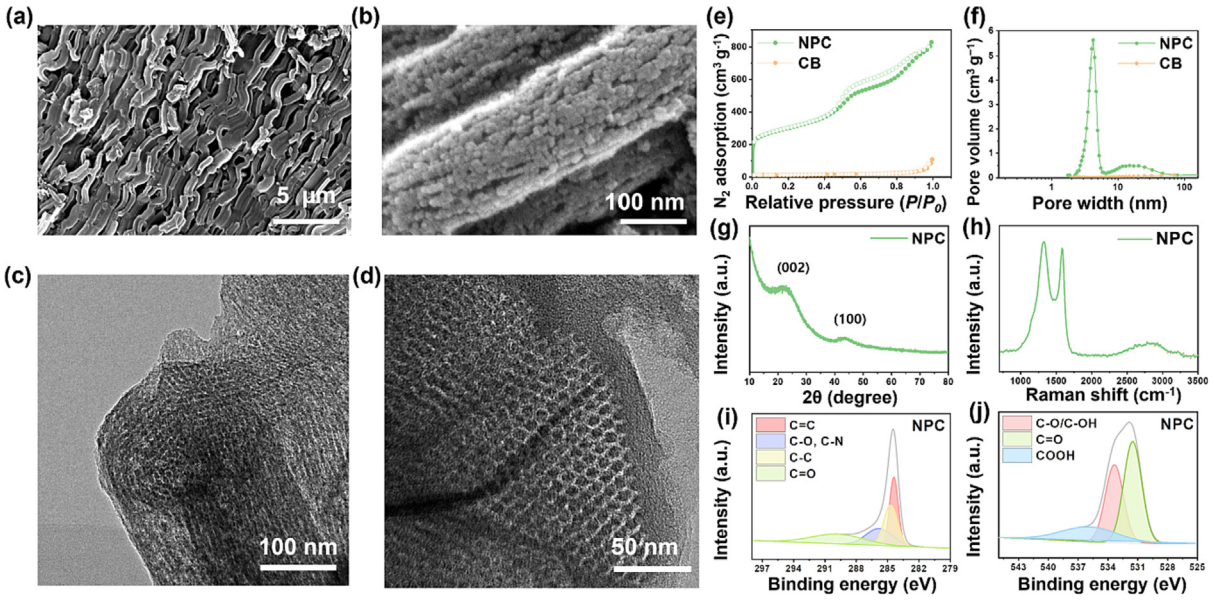

Fig. 1. Material properties of the NPCs. (a, b) FE-SEM and (c, d) FE-TEM images of the NPCs at different magnifications. (e) Nitrogen adsorption–desorption isotherms and (f) pore size distribution of the NPCs and CBs. (g) XRD pattern and (h) Raman spectrum of the NPCs. XPS (i) C 1*s* and (j) O 1*s* profiles of the NPCs.

dendritic metal growth [19,31]. The dendritic metal growth on SS electrode was confirmed by *ex situ* FE-SEM observation after aluminum metal deposition of 1.0 mAh cm^{-2} at 1.0 mA cm^{-2}, which is clearly distinctive from those of the CB and NPC electrodes (Fig. S7). Spontaneous supply of aluminum charge carriers reduces the concentration polarization and can therefore be a key for uniformly depositing aluminum with no dendrite growth. The η_e values, which include the concentration polarizations, are shown at different SoCs for the NPC, CB, and SS electrodes (Fig. S8). Fig. S8 reveals that the NPC electrodes had lower η_e values with scant concentration polarization at different current densities and SoCs, which indicates the superiority of the NPC electrodes. To more clarify the effects of pore structure and surface area on both η_n and η_e values, a previously reported NPC electrode (called as NPC-2.5) that has much higher specific surface area of ~2315 m^2 g^{-1}, pore width of ~2.5 nm, and complex pore geometry was prepared and its electrochemical performances were compared with those of the NPC electrode (Fig. S9) [32]. The η_n value of the NPC-2.5 was confirmed as ~17.4 mV which is more than twice of that (~7.1 mV) in the NPC electrode (Fig. S9c). In addition, the NPC-2.5 shows a higher η_e value during aluminum metal deposition/dissolution process (Fig. S9d). This result indicates that pore size and geometry rather than specific surface area are keys for improving the electrochemical performance of the NPC electrode. Additionally, the effects of surface property and carbon microstructure were confirmed by comparing the η_n and η_e values of the NPC electrode with the high-temperature annealing sample prepared at 1600 °C, called as NPC-1600. The carbon microstructure of the NPC electrode was more developed, and accordingly, surface oxygen contents were reduced by O/C ratio of 0.01 with the thermal treatment (Fig. S10a–d). The more developed graphitic structure of the NPC-1600 electrode is, however, counter-productive for the electrochemical performances (Fig. S10e and f). This could be due to a reduction of wettability in the ionic liquid-based electrolyte (Fig. S11), which could decrease effective surface area, leading to the increased η_n and η_e values.

The deposition of aluminum progresses on the surface of the negatively charged electrode *via* the nucleation reaction with four molecular anions and three electrons, as shown in Eq. (1). To understand the mechanism of the cathodic reaction in detail, it is necessary to consider the following elementary reaction steps: (i) an aluminum reduction process in which the $Al_2Cl_7^-$ anion releases Al atoms onto the electrode surface by electron transfer and the remaining $AlCl_4^-$ and $3Cl^-$ anions into the surroundings (Eq. (2)), and (ii) an anion conversion process in which the three released Cl^- anions are complexed with three adjacent $Al_2Cl_7^-$ anions, which are then converted to six $AlCl_4^-$ anions (Eq. (3)).

$$Al_2Cl_7^- + 3e^- \rightarrow Al + AlCl_4^- + 3Cl^- \quad (2)$$

$$3Cl^- + 3Al_2Cl_7^- \rightarrow 6AlCl_4^- \quad (3)$$

In the first elementary step (Eq. (2)), an excessive amount of chloride anions with a high charge density is generated, which strongly perturbs the charge neutrality. This induces an abrupt thermodynamic instability in the reaction environment, which may serve as a major source of overpotential for nucleation. Thus, the overall reactivity of Al nucleation can be determined according to the speed at which these excess chloride anions form $AlCl_4^-$ (Eq. (3)) by lowering the average charge density of the anions to minimize the Coulomb repulsion. From the previously reported formation tendency for chloroaluminate anions, based on the ratio of Cl^- to $AlCl_3$, the chemical equilibrium can shift from $Al_2Cl_7^-$ to $AlCl_4^-$ by locally increasing the Cl^- concentration [33]. Consequently, the local anion concentration at the negative electrode increases by 1.75 times. The overall charge balance with the positive-electrode region can thus be obtained by fast Cl^- transfer based on the Grotthuss mechanism through the chloroaluminate anion network [34]. Therefore, it is presumed that these series of reactions will proceed preferably under conditions with a higher collision frequency between anionic species.

To confirm that the structural features of the well-ordered NPC material can increase the collision frequency between anionic species, the dynamic behaviors of ionic liquid molecules depending on the nanoscale surface structure were calculated using MD simulations. The schematic illustration and the as-built nanogap capacitor models of the EMIm-Al_2Cl_7 electrolyte and flat/trench/well-type graphite electrodes were shown in Fig. 3(a) and Fig. S12. The dynamic behaviors of the ionic liquid molecules on the three types of negative electrode surfaces were analyzed according to

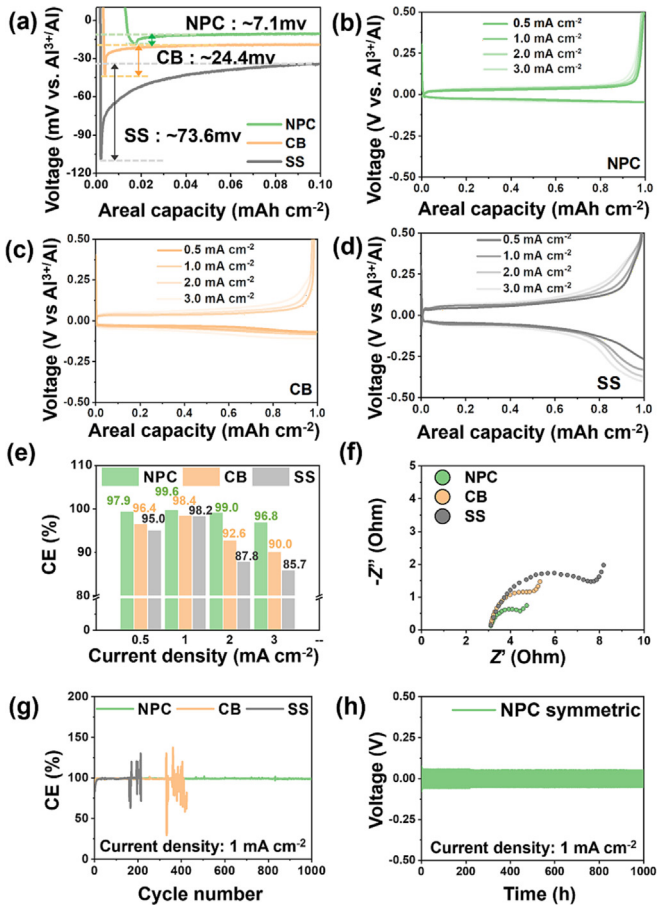

Fig. 2. Electrochemical performance of the NPC, CB, and SS electrodes in an electrolytic solution of $AlCl_3$ and ethyl-3-methylimidazolium tetrachloroaluminate ($EMImAlCl_4$) (1.0:1.3 molar ratio) and at a cut-off capacity of 1 mAh cm^{-2}. (a) Profiles of galvanostatic deposition of aluminum on NPC, CB, and SS electrodes at 50 μA cm^{-2}, and galvanostatic aluminum deposition-dissolution profiles for the (b) NPC, (c) CB, and (d) SS electrodes at 0.5, 1.0, 2.0, and 3.0 mA cm^{-2}. (e) CE versus current densities of the NPC, CB, and SS electrodes. (f) EIS profiles of the NPC, CB, and SS electrodes at frequencies between 50 mHz and 1 MHz after depositing aluminum at 1 mAh cm^{-2}. (g) Cycling performance of the NPC, CB, and SS electrodes at 1 mA cm^{-2} in half-cells, and (h) galvanostatic discharge–charge profiles of the symmetric cell, which was composed of two same NPC electrodes including aluminum of 2 mAh cm^{-2}.

the charging conditions. Fig. 3(b) shows the number density distribution of the ionic liquid molecules along the normal direction of the negative electrode surface. In uncharged conditions, cations and anions are evenly distributed to balance the charges in the electrical double-layer (EDL) region on each type of surface. Under negatively charged conditions, the cation density adjacent to the electrode surface increases, while the anion density decreases. However, owing to the structural characteristics of the EDL composed of only ionic components, an anion concentration still exists near the negative electrode surface, which facilitates Al reduction. The diffusion coefficient of the anionic species was analyzed through the calculation of the mean squared displacement to determine the differences in the collision behavior of anions on each surface. Since the collision frequency is inversely proportional to the diffusion coefficient [35], lower diffusivities result in a higher collision probability.

The diffusion coefficient of anions depending on the surface charge density within 5 nm from the bottom surface of each electrode is depicted in Fig. 3(c). Under uncharged conditions, the anion diffusivity at the flat surface is 2.74×10^{-6} cm^2 s^{-1}, whereas those of the trench- and well-type surfaces are reduced by 37% and 66%, respectively, compared to that of the flat surface. The diffusion coefficient decreases almost linearly as the order of geometric confinement increases, which is observed with the one-dimensional constraint for trench-type surface and the two-dimensional constraint for well-type surface. These quenched diffusion behaviors within the nanoscale geometric confinement can facilitate collisions between anionic species, enabling the fast chemical equilibration of the chloroaluminate anion complexes. This tendency is also observed for cationic diffusion (Fig. S13). Contrary to expectations, surface charging does not have a significant effect on the diffusion, implying that the dynamics of the ionic components is not easily perturbed by the distributed charges on the electrode surface. Therefore, Al nucleation from adjacent anions likely occurs in the confined nanopores, which lowers the η_n value and increases the rate capabilities with a lower concentration polarization by facilitating anionic collisions.

Because of the nanoconfinement effect, the NPC electrodes showed the highest CE of ~99.6% at an areal current density of 1 mA cm^{-2}, and the difference in the CE of the NPC electrode versus the other electrodes increased with increasing areal current densities (Fig. 2e). The electrochemical impedance spectroscopy (EIS) data also revealed that the charge-transfer resistance of the NPC electrodes was lower than that of the CB and SS electrodes (Fig. 2f). In addition, the NPC electrodes showed stable and long-term cycling performance over 1000 cycles at an areal current density of 1 mA cm^{-2}, with a cut-off capacity of 1 mAh cm^{-2} (Fig. 2g). This result is superior to that obtained with the CB and SS electrodes under the same cycling conditions; these electrodes showed

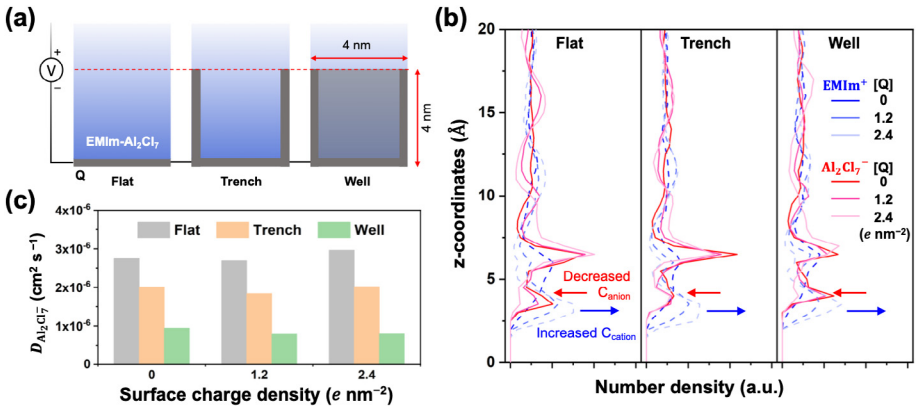

Fig. 3. Molecular dynamics simulation results. (a) Schematic illustration of the three types of the electrode surface. (b) Number density distributions of cationic and anionic species at each electrode surface depending on the surface charge density. (c) Nanoconfinement and charging effect on the diffusion coefficients of anionic species.

sudden cycling decays after ~310 and ~170 cycles, respectively. Moreover, the cycling data for the symmetric cells, which were assembled with two identical NPC electrodes including an aluminum mass loading of 2 mAh cm^{-2}, supported the stable cycling performance of the NPC-guided AMA (Fig. 2h). In the symmetric cell test at an areal current density of 1 mA cm^{-2} with a cut-off capacity of 1 mAh cm^{-2}, the initial low η_e value was well-maintained during 1000 repetitive cycles. Therefore, because of the nanoconfinement effect, the NPC electrodes afforded better round-trip efficiencies and cycling stability.

To confirm the nanoconfinement effect of the NPC electrode, *ex situ* FE-TEM analyses with energy dispersive X-ray spectroscopy (EDS) were performed after aluminum metal deposition at 1 mAh cm^{-2} (Fig. 4a and Fig. S14). To minimize exposure of the aluminum-containing NPC samples to air, a 2032-type coin cell was assembled with the TEM grid on which the NPC particles were mounted, as shown in Fig. S15. The cell was then discharged until aluminum was deposited at 1 mAh cm^{-2}. After discharge, the TEM grid was extracted from the cell and washed with a solution of anhydrous acetonitrile. A thoroughly sealed container was used for FE-TEM analysis. During the FE-TEM analysis, the sample was exposed to air for only a few seconds. The *ex situ* FE-TEM image shows multitudinous nanoparticles with diameters of approximately 2–3 nm throughout the interior area of the NPC particles (Fig. 4a and Fig. S14). The selected area electron diffraction (SAED) pattern revealed that the nanoparticles comprised aluminum with (111), (200), (220), (311) and (222) planes (Fig. 4b). After stripping the deposited metal, the nanoparticles were reversibly removed from the internal area of the NPC particles (Fig. 4c and Fig. S16), where the SAED profile showed a broad ring pattern of the NPC with no aluminum nanoparticles (Fig. 4d). Note that the *ex situ* EDS mapping images revealed that a large amount of aluminum-containing anions was present throughout the entire area of the NPC after full discharge (Fig. S17). This result indicates that as the charge carriers were concentrated in the confined nanopores, the deposition-dissolution of aluminum was likely progressively reversed. *Ex situ* nitrogen adsorption–desorption isotherms were acquired after depositing aluminum on the NPC sample. To obtain a convincing result, ~0.1 g of the aluminum-containing NPC particles was collected from several coin-cells, and the pore structure of the aluminum-deposited NPC samples was characterized at −196 °C. The *ex situ* pore size distribution curves obtained from the nitrogen isotherms revealed that the peak intensity of the nanopores centered at ~4 nm was significantly reduced after aluminum deposition (Fig. 4e). After the aluminum was stripped, the peak corresponding to the nanopores became more intense, demonstrating that deposition-dissolution of aluminum in the confined nanopores was reversible. In addition, the nanoporous structure was well-maintained after consecutive 50 cycles. This result clearly indicates that the nanopores were filled with deposited aluminum, which was reversibly removed. The *ex situ* XPS depth profile confirmed this high reversibility (Fig. 4f) [36]. After 500 aluminum deposition-dissolution cycles, the NPC was extracted from the tested cell and washed with a solution of anhydrous acetonitrile. *Ex situ* XPS depth analysis of the purified NPC sample showed that the internal area of the nanoporous structure had a high carbon content of over 70 at.%. This finding suggests that the carbon surfaces were well-maintained without forming a passivation layer from the side reactions, which demonstrates that the NPC electrode exhibits excellent cycling stability of the over long-term. Additionally, *ex situ* XRD and *ex situ* Raman spectra characterizations were carried out after the aluminum deposition of 1 mAh cm^{-2} and followed by dissolution (Fig. 4g and h). In the *ex situ* XRD pattern after aluminum deposition, the Al(111) and Al(200) peaks were exhibited at around 38.5° and 44.7°, respectively, with the broad graphite(002) peak, where the size of the deposited aluminum metals was calculated as ~3.8 nm through the Scherrer equation (Fig. 4g). The calculated metal size is similar to the pore size of the NPC electrode, supporting the results in the *ex situ* FE-TEM image as shown in Fig. 4(a) and the *ex situ* pore size distribution curves (Fig. 4e). In addition, the aluminum peaks were reversibly removed, while the graphite(002) peak was well-maintained after the aluminum dissolution process, indicating that the carbon structure of the NPC electrode was slightly affected during the aluminum deposition-dissolution cycle (Fig. 4g). Furthermore, the *ex situ* Raman spectra confirm that the carbon microstructure of the NPC electrode did not change in the aluminum metal deposition-dissolution process (Fig. 4h).

3. Experimental

Preparation of NPC electrode: The NPCs were prepared using a previously reported method, which consisted of a two-step fabrication procedure [29]. In the first step, Pluronic P123 (4 g, Sigma-Aldrich) was dissolved in a mixture of HCl (25 g, Daejung Co.) and distilled water (130 g) at 35 °C. Tetraethyl orthosilicate (8.5 g, Alfa Aesar) was then dissolved in the mixture and stirred for 24 h. The solution was placed in a convection oven for 24 h at 100 °C. After the solution was vacuum-filtered, the products, which were not washed, were calcined in a tube furnace under air at 550 °C at a heating rate of 5 °C min^{-1}, and the products were held at the target temperature for 6 h. The final product, SBA-15, was obtained from the first step. In the second step, as-prepared SBA-15 (1 g) was dissolved in distilled water (5 g) with sucrose (1.25 g, Sigma-Aldrich) and sulfuric acid (0.09 g, Duksan). The mixture was then aged in a convection oven at 100 °C for 12 h and then at 160 °C for 12 h. The same thermal treatments (100 °C for 12 h, followed by 160 °C for 12 h) were successively conducted after adding sucrose (0.8 g), sulfuric acid (0.09 g), and distilled water (5 g) to the mixture. The resulting powders were heated to 900 °C under nitrogen, at a flow rate of 100 mL min^{-1}. A heating rate of 5 °C min^{-1} was applied and the sample was held at the target temperature for 2 h. After cooling to room temperature, the products were immersed in 5 wt.% hydrofluoric acid (Duksan) at room temperature for 12 h to eliminate the SBA-15 template. Finally, the NPCs were obtained after washing with distilled water and ethanol several times.

Characterization: Field-emission scanning electron microscopy (S-4300, Hitachi, Japan) and FE-TEM (JEM2100F, JEOL, Japan) images were acquired to characterize the morphology of the NPCs and CBs. Nitrogen adsorption–desorption isotherms (ASAP 2020, Micromeritics, USA) were acquired at −196 °C to characterize the porous structures of the NPCs and CBs. High-resolution FE-TEM images were acquired to visualize the nanopores. XRD (Rigaku D/MAX 2500, Rigaku, Japan) and Raman spectroscopy (514.5 nm, 2.41 eV, and 16 mW) were used to analyze the carbon microstructures of the NPCs and CBs. XPS (PHI 5700 ESCA, USA) was used to investigate the chemical properties of the surface of the NPCs and CBs. Electrochemical tests were conducted using 2032-type coin cells and automatic battery cyclers (WBCS3000, Wonatech, Korea). The coin cells were sealed with a Kapton polyimide tape which has a hole (1/2 inch in diameter) in the center as shown in Fig. S18. The working electrodes were prepared by the slurry method using 90 wt.% of NPC or CB. This method involved mixing 10 wt.% of a polyvinylidene fluoride (PVDF, Sigma-Aldrich, USA) binder in an *N*-methyl-2-pyrrolidone solution. Bar coating was then used to homogeneously coat the solution onto a SS foil (0.025 mm, Alfa aesar, USA). The electrodes (1/2 inch in diameter) were punched, and the active material loading density was controlled at ~1 mg cm^{-2} for each electrode. The coin cells were assembled in a glovebox filled with argon gas. The NPCs, CBs, or SSs were used

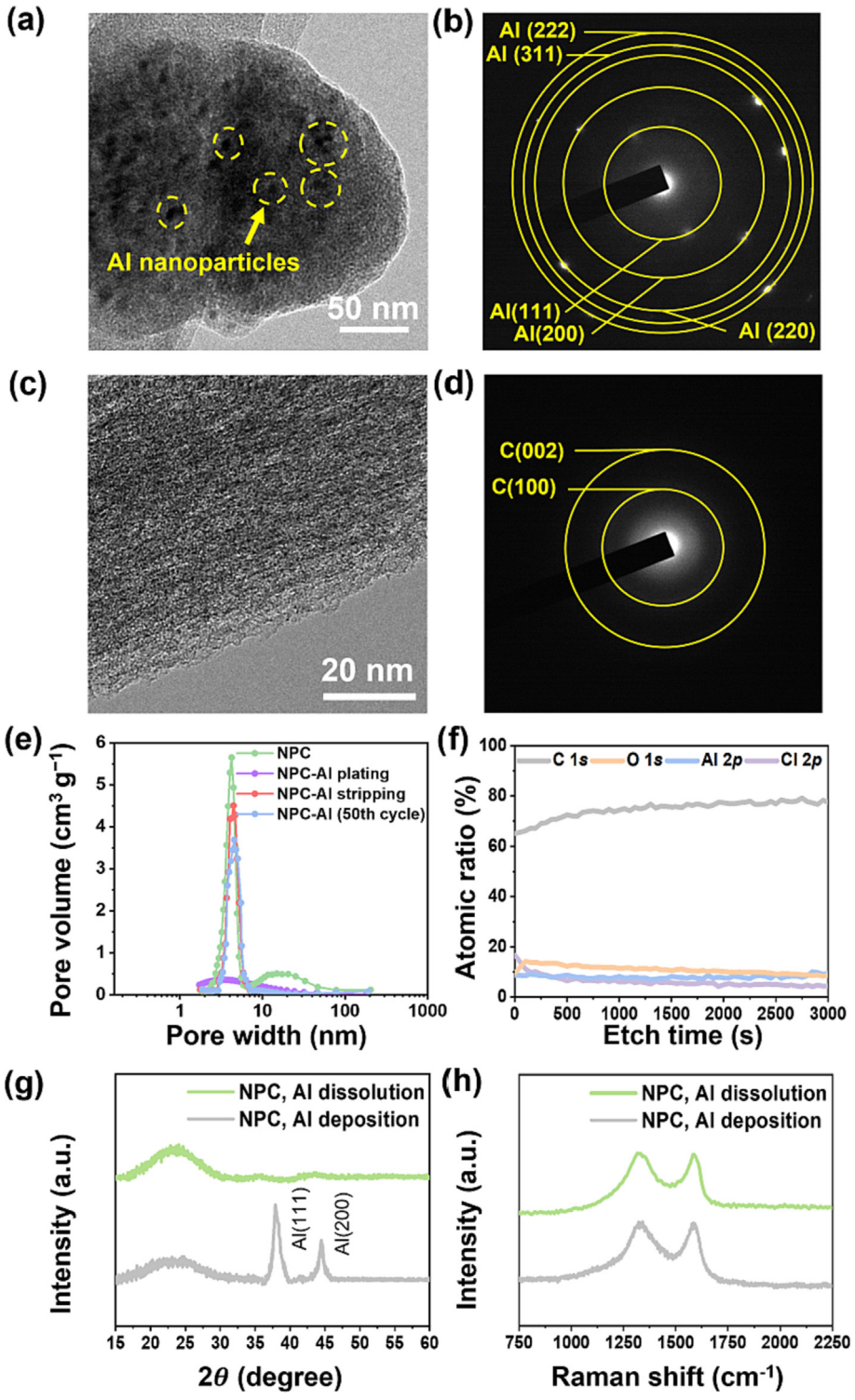

Fig. 4. *Ex situ* analysis of the NPC electrodes. *Ex situ* FE-TEM images of the NPC electrode (a) after depositing aluminum of 1 mAh cm^{-2} and (c) its subsequent extraction. SAED patterns of the NPC electrode (b) after depositing aluminum of 1 mAh cm^{-2} and (d) its subsequent extraction. (e) Pore size distribution of the pristine NPC, aluminum-deposited NPC, aluminum-extracted NPC, and NPC electrodes after 50th aluminum deposition-dissolution cycle. (f) XPS depth profiles of the NPC electrode after 500 aluminum deposition-dissolution cycles. (g) *Ex situ* XRD patterns and (h) *ex situ* Raman spectra of the NPC electrodes after aluminum deposition of 1 mAh cm^{-2} and followed by dissolution.

as the working electrode, while aluminum (Sigma-Aldrich, USA) was used as both the reference and counter electrodes. A glass microfiber filter (GF/F, Whatman, US) was used as the separator. Symmetric cells were assembled with two identical NPCs, which included aluminum that was electrochemically pre-deposited in a half-cell configuration at 2 mAh cm^{-2}.

Computational details: Molecular dynamics simulations were carried out using the Large-Scale Atomic-Molecular Massively Parallel Simulator (LAMMPS) package [37] with the OPLS all-atom forcefield optimized for ionic liquids [38]. All simulations were carried out using the Nose-Hoover thermostat [39] to maintain the temperature at 400 K. The 4 nm × 4 nm graphene sheet structures

were used for the positive and negative electrodes, and the partial charges corresponding to the surface charge density of 0.0, 1.2 and 1.4 e nm^{-2} were applied. The diffusion coefficient of ionic species was calculated based on the mean squared displacement for 1.0 ns trajectories.

4. Conclusions

NPC electrodes comprising well-developed nanopores (~4 nm in diameter) and amorphous carbon structures with oxygen functional groups (O/C ratio: ~0.04) were prepared. The electrochemical performance of aluminum-loaded NPC as an AMA was compared with that of macroporous CB and 2D SS electrodes. The initial η_n value of the NPC electrode was reduced by ~7.1 mV compared with that (~24.4 and ~73.6 mV) of the CB and SS electrodes, confirming that the NPC electrode more effectively catalyzed the nucleation of aluminum. In addition, the NPC electrode led to lower η_e values with remarkably lower concentration polarization at different current densities and SoCs, confirming superior growth of aluminum in the NPC electrodes. The MD simulation results showed that the quenched dynamics of electrolyte molecules in the confined nanopores drive the fast chemical equilibrium of anionic species due to facilitated anionic collisions, which lowers the η_n value. *Ex situ* FE-TEM observation revealed the presence of numerous aluminum nanoparticles in the multiple confined nanopores, demonstrating the nanopore-based nucleation and growth of aluminum. In the large number of confined nanopores, the concentrated charge carriers are easily nucleated into the metallic phase, where multitudinous nanoparticles are plausibly simultaneously formed. This significantly lowered the effective current density. Because of the nanoconfinement effect, higher CE values were achieved at different areal current densities and SOCs. More stable cycling behavior was confirmed over 1000 cycles in both the half-cell and symmetric cell tests.

Declaration of competing interest

The authors declare that they have no known competing financial interests or personal relationships that could have appeared to influence the work reported in this paper.

Acknowledgments

This work was supported by the Basic Science Research Program through the National Research Foundation of Korea (NRF) Funded by the Ministry of Education (NRF-2019R1A2C1084836, NRF-2018M1A2A2061994, and NRF-2021R1A4A2001403) and the KU-KIST School Program.

Appendix A. Supplementary data

Supplementary data to this article can be found online at https://doi.org/10.1016/j.jechem.2022.06.048.

References

[1] G.A. Elia, K. Marquardt, K. Hoeppner, S. Fantini, R. Lin, E. Knipping, W. Peters, J.-F. Drillet, S. Passerini, R. Hahn, Adv. Mater. 28 (2016) 7564–7579.
[2] J. Bitenc, N. Lindahl, A. Vizintin, M.E. Abdelhamid, R. Dominko, P. Johansson, Energy Storage Mater. 24 (2020) 379–383.
[3] C. Li, Z. Sun, T. Yang, L. Yu, N. Wei, Z. Tian, J. Cai, J. Lv, Y. Shao, M.H. Rümmeli, J. Sun, Z. Liu, Adv. Mater. 32 (2020) 2003425.
[4] H. Tian, T. Gao, X. Li, X. Wang, C. Luo, X. Fan, C. Yang, L. Suo, Z. Ma, W. Han, C. Wang, Nat. Commun. 8 (2017) 14083.
[5] Z. Yi, G. Chen, F. Hou, L. Wang, J. Liang, Adv. Energy Mater. 11 (2021) 2003065.
[6] H. He, H. Tong, W. Song, X. Song, J. Liu, J. Mater, Chem. A. 8 (2020) 7836–7846.
[7] N. Jayaprakash, S.K. Das, L.A. Archer, Chem. Commun. 47 (2011) 12610–12612.
[8] D.J. Kim, D.-J. Yoo, M.T. Otley, A. Prokofjevs, C. Pezzato, M. Owczarek, S.J. Lee, J. W. Choi, J.F. Stoddart, Nat. Energy. 4 (2019) 51–59.
[9] M.-C. Lin, M. Gong, B. Lu, Y. Wu, D.-Y. Wang, M. Guan, M. Angell, C. Chen, J. Yang, B.-J. Hwang, H. Dai, Nature 520 (2015) 325.
[10] S. Wang, S. Huang, M. Yao, Y. Zhang, Z. Niu, Angew. Chem. Int. Ed. 59 (2020) 11800.
[11] F. Ambroz, T.J. Macdonald, T. Nann, Adv. Energy Mater. 7 (2017) 1602093.
[12] G. Li, M. Kou, J. Tu, Y. Luo, M. Wang, S. Jiao, Chem. Eng. J. 421 (2021) 127792.
[13] T. Zhang, T. Cai, W. Xing, T. Li, B. Liang, H. Hu, L. Zhao, X. Li, Z. Yan, Energy Storage Mater. 41 (2021) 667–676.
[14] G. Wang, E. Dmitrieva, B. Kohn, U. Scheler, Y. Liu, V. Tkachova, L. Yang, Y. Fu, J. Ma, P. Zhang, F. Wang, J. Ge, X. Feng, Angew. Chem.-int. Edit. 61 (2022) 202116194.
[15] S. Ha, J.C. Hyun, J.H. Kwak, H.-D. Lim, B.S. Youn, S. Cho, H.-J. Jin, H.-K. Lim, S.M. Lee, Y.S. Yun, Chem. Eng. J. 437 (2022) 135416.
[16] Q. Zhao, J. Zheng, Y. Deng, L. Archer, J. Mater. Chem. A. 8 (2020) 23231–23238.
[17] J.M. Griffin, A.C. Forse, W.Y. Tsai, P.L. Taberna, P. Simon, C.P. Grey, Nat. Mater. 14 (2015) 812–819.
[18] C. Merlet, B. Rotenberg, P.A. Madden, P.-L. Taberna, P. Simon, Y. Gogotsi, M. Salanne, Nat. Mater. 11 (2012) 306–310.
[19] D. Lin, Y. Liu, Y. Cui, Nat. Nanotechnol. 12 (2017) 194–206.
[20] X.B. Cheng, R. Zhang, C.Z. Zhao, Q. Zhang, Chem. Rev. 117 (2017) 10403–10473.
[21] C. Niu, H. Pan, W. Xu, J. Xiao, J.-G. Zhang, L. Luo, C. Wang, D. Mei, J. Meng, X. Wang, Z. Liu, L. Mai, J. Liu, Nat. Nanotechnol. 14 (2019) 594–601.
[22] S. Ha, H.J. Yoon, J.I. Jung, H. Kim, S. Won, J.H. Kwak, H.-D. Lim, H.-Y. Jin, J.J. Wae, Y.S. Yun, Energy Storage Mater. 37 (2021) 567–575.
[23] J. Zheng, D.C. Bock, T. Tang, Q. Zhao, J. Yin, K.R. Tallman, G. Wheeler, X. Liu, Y. Deng, S. Jin, A.C. Marschiok, E.S. Takeuchi, K.J. Takeuchi, L.A. Archer, Nat. Energy. 6 (2021) 398–406.
[24] N. Lindahl, J. Bitenc, R. Dominko, P. Johansson, Adv. Funct. Mater. 30 (2020) 2004573.
[25] Z. Liu, J. Wang, H. Ding, S. Chen, X. Yu, B. Lu, ACS Nano. 12 (2018) 8456–8466.
[26] E. Zhang, J. Wang, B. Wang, X. Yu, H. Yang, B. Lu, Energy Storage Mater. 23 (2019) 72–78.
[27] M.C. Lin, M. Gong, B. Lu, Y.P. Wu, D.Y. Wang, M.Y. Guan, M. Angell, C.X. Chen, J. Yang, B.J. Hwang, H.J. Dai, Nature. 520 (2015) 324–328.
[28] S. Park, H.-J. Jin, Y.S. Yun, Adv. Mater. 32 (2020) 2002193.
[29] S. Jun, S.H. Joo, R. Ryoo, M. Kruk, M. Jaroniec, Z. Liu, T. Ohsuna, O. Terasaki, J. Am. Chem. Soc. 122 (2000) 10712–10713.
[30] S.Y. Cho, Y.S. Yun, D. Jang, J.W. Jeon, B.H. Kim, S. Lee, H.-J. Jin, Nat Commun. 8 (2017) 74.
[31] S. Ha, D. Kim, H.-K. Lim, C.M. Koo, S.J. Kim, Y.S. Yun, Adv. Funct. Mater. 31 (2021) 2101261.
[32] S. Moon, D.-H. Kim, J.H. Kwak, S.M. Lee, H.-D. Lim, K. Kang, H.-J. Jin, Y.S. Yun, Appl. Surf. Sci. 537 (2021) 148037.
[33] S. Takahashi, K. Suzuya, S. Kohara, N. Koura, L.A. Curtiss, M.-L. Saboungi, Z. Phys, Chem. 209 (1999) 209–221.
[34] B. Kirchner, A.P. Seitsonen, Inorg. Chem. 46 (2007) 2751–2754.
[35] Y.-C. Liu, Q. Wang, X.-F. Li, J. Chem. Phys. 122 (2005) 044714.
[36] J. Ge1, L. Fan, A.M. Rao, J. Zhou, B. Lu, Nat. Sustain. 5 (2022) 225–234.
[37] S. Plimpton, J. Comput. Phys. 117 (1995) 1–19.
[38] S.V. Sambasivarao, O. Acevedo, J. Chem. Theory Comput. 5 (2009) 1038–1050.
[39] D.J. Evans, B.L. Holian, J. Chem. Phys. 83 (1985) 4069.